

MERGE OR SURVIVE: NUMBER OF POPULATION III STARS PER MINIHALO

HAJIME SUSU

Department of Physics, Konan University, Okamoto, Kobe, Japan
Draft version March 16, 2022

ABSTRACT

The formation process of Population III (PopIII) stars in the mass accretion phase is investigated by numerical experiments. The barotropic relation of primordial gas and artificial stiffening of the equation of state in very dense regions ($> 10^{15} \text{ cm}^{-3}$) enables us to follow the fragmentation of PopIII circumstellar disks and the merging processes of the fragments. The disk becomes gravitationally unstable to fragmentation, followed by a rapid merger process typically within 100 yrs, which roughly corresponds to one orbital time of the circumstellar disk. We also find that the fragmentation of the gas disk around a multiple system, a circumbinary disk, is rare; however, it is frequent in the disk around an individual protostar. We also perform a simulation with standard sink particles, where the number and total mass of sink particles are in rough agreement with those of the stiff equation of state runs. Based on the results of these numerical results, we model the evolution of the number of fragments with a simple phenomenological equation. We find that the average number of fragments is roughly proportional to $t^{0.3}$, where t is the elapsed time since the formation of the first protostar. Next, we compare this trend with a number of published numerical studies by scaling the elapsed time according to the scale-free nature of the system. As a result, we find most of the results in the literature agree well with the relation. Present results combined with the previous studies in the literature imply that the PopIII stars tend to be born not as single stars, but in multiple systems.

Keywords: early Universe—radiative transfer—first stars—metal poor stars

1. INTRODUCTION

Formation theory of the first stars predicts that very massive star formation of mass $M \gtrsim 100 M_{\odot}$ is preferred in primordial environments (Omukai & Nishi 1998). In the Λ CDM paradigm, those stars form in minihalos of $M \sim 10^6 M_{\odot}$ at $z \sim 20 - 40$ (e.g., Haiman et al. 1996; Nishi & Susa 1999; Fuller & Couchman 2000; Abel et al. 2002; Bromm et al. 2002; Yoshida et al. 2003). Pristine gas in the minihalos cool via H_2 line cooling, which is significantly less efficient than cooling by heavier elements and dust. As a result, the gas temperature is higher than the present-day counterpart by two orders of magnitude. For the gas cloud to collapse, the mass of the cloud should exceed the Jeans mass, which is larger for higher temperatures. Consequently, the mass of the collapsing primordial gas is of the order of $10^3 M_{\odot}$ at $\sim 10^4 \text{ cm}^{-3}$, while it is $\sim 1 M_{\odot}$ in the local environment. Therefore, it seems to be reasonable that very massive stars are preferred in the primeval environment as a first approximation.

On the other hand, recent numerical simulations of the mass accretion phase predict that the disk around the primary protostar fragments into multiple pieces that could culminate in binaries, triplets, etc. Thus, the number of these fragments per minihalo increases, and the mass distribution of them also changes dramatically (Stacy et al. 2010, 2012, 2016; Clark et al. 2011; Greif et al. 2011, 2012; Smith et al. 2011; Hirano & Bromm 2017). These fragments, the population III (PopIII) protostars, could be less massive than $100 M_{\odot}$, or even less than $0.8 M_{\odot}$, which could survive until the present. To test for the presence of such low-mass stars, it is useful to search for the zero-metallicity stars in our

galaxy (Hartwig et al. 2015a; Ishiyama et al. 2016; Griffen et al. 2018; Magg et al. 2018, 2019). It is also important to match the theoretical initial mass function (IMF) to the abundance ratio observed on the extremely metal poor (EMP) stars (e.g. Susa et al. 2014; Ishigaki et al. 2018), because they could be born in the remnants of first stars (e.g., Smith et al. 2015; Chen et al. 2017; Chiaki et al. 2018). Such efforts can constrain the mass distribution of the first-generation stars. In any case, it is crucial to have a good theoretical assessment of the mass distribution of the PopIII stars to compare with observations.

However, the number of the protostars per minihalo and the mass distribution of them are still unclear from numerical studies. The final mass of the fragment depends fundamentally on the radiative feedback by the protostars themselves, which requires long integration times. The feedback arises after the protostars have grown to $15 - 20 M_{\odot}$, which corresponds to several thousand years after the formation of the first protostar. After the onset of the radiative feedback, the accreting gas is heated by the UV radiation and evaporated. Finally, the gas accretion onto the protostars is shut off to yield the final mass of the protostars. This result can only be achieved by coarse radiation-hydrodynamics simulations, which cannot trace the detailed fragmentation and merger processes at the beginning of protostar formation (Hosokawa et al. 2011; Stacy et al. 2012; Susa 2013; Susa et al. 2014; Hirano et al. 2014, 2015; Stacy et al. 2016; Hosokawa et al. 2016).

Alternatively, high resolution simulations that resolve the initial phase of the protostar formation, reveal that the fragmentation of the accretion disk as well as the merging of the fragments are quite common, though only for about 10-100 yrs after primary protostar formation

can be traced because of the high numerical cost. For instance, the highest resolution cosmological simulation by Greif et al. (2012), without sink particles, has shown that $\sim 1/3$ of the formed fragments survive until ~ 10 yrs after the formation of the primary protostar, while another $\sim 2/3$ merge with each other. They predict that about four fragments survive on average through the simulated time. Machida & Doi (2013) also have performed similar calculations to find ~ 10 fragments, and many of them merge in their nested-grid highest resolution box, but some are ejected to outer low-resolution regions where their fate cannot be traced.

Sink particle simulations also predict fragmentation of the disk, and they follow relatively longer time scales than non-sink simulations. For example, Stacy et al. (2016) trace the evolution of a single minihalo for 5000 yrs, and they also include the effects of ultraviolet radiative feedback by the forming protostars, in the later phase of the evolution. They predict 37 sinks, that is, protostars, are expected in a minihalo. However, the differences in numerical methods, i.e., the calculations with or without sink particles, might affect the final results.

In addition, all non-sink/sink simulations introduce an artificial threshold density above which the gas clump is replaced by a sink particle or the equation of state becomes stiff to avoid the very short time scale inside the protostars¹. This threshold density is very different among studies, depending on the time scale that each author tries to resolve. As a result, the results are so diverse that it is difficult to derive a universal law of fragmentation of PopIII accretion disks.

In this study, we perform another simple hydrodynamics simulation with and without sink particles to investigate the formation and merger of the fragments in the accretion disk surrounding protostars in a primordial environment. We analyze the numerical results in detail, and compare them with a number of published results by using a scaling relation. Utilizing all the numerical results so far, we infer the final number of fragments in the minihalos.

2. METHODOLOGY

2.1. Simulations without sinks

We employ the standard SPH scheme to calculate the dynamics of a collapsing gas cloud. The code used in this study is based on RSPH (Susa & Umemura 2004; Susa 2006), designed to solve the chemical network as well as the radiative cooling/heating/transfer of primordial gas. In this study, the chemistry/cooling/transfer solvers are switched off. Instead, we simply assume the barotropic relation between the density and the temperature of the gas cloud to save computational time. The barotropic equation of state is pre-calculated by a one-zone model (Susa et al. 2015) and tabulated to be used in the hydrodynamics simulations.

Because we are interested in the mass-accretion phase, we have to set a threshold hydrogen number density, n_{th} , above which the gas becomes stiff against further collapse. In the present study, we set the threshold density at $n_{\text{th}} = 10^{15} \text{ cm}^{-3}$, above which the relation $T \propto n_{\text{H}}^{\gamma_{\text{eff}}-1}$

¹ One exception is the calculation by Greif et al. (2012). They solve the radiative transfer of cooling photons, thereby introducing the threshold density naturally.

Table 1
Summary of numerical parameters

cloud mass	$1.88 \times 10^3 M_{\odot}$
initial angular velocity	$2 \times 10^{-14} \text{ s}^{-1}$
rotation axis	randomly chosen for R1-R5 runs
initial central density	$1.4 \times 10^4 \text{ cm}^{-3}$
initial central temperature	196 K
$m = 2$ perturbation	$\delta = 0.1$
maximal mass resolution	$0.014 M_{\odot}$
n_{th}	10^{15} cm^{-3}

Note. — Numerical parameters for R1-R5 and an SPH run. SPH run uses identical initial condition of R1.

holds, where $\gamma_{\text{eff}} = 5$. This very stiff equation of state is employed in opposition to the sink particles simulations, which introduce a “hole” around the sinks.

The initial condition of the simulation is a Bonnor-Ebert sphere around the critical density of H_2 level transition, which mimics the “loitering” primordial gas cloud found in cosmological simulations (Abel et al. 2002; Yoshida et al. 2003). The particle distribution is created as follows. First, we put particles in a box to relax until the system settles down to a uniform and equilibrium state. As a result, we have a glass-like nearly uniform particle distribution instead of an aligned distribution on grid points. The density fluctuation due to the glass-like distribution is $\lesssim 3\%$. Then, we hollow out a spherical region. Finally, the radial distribution of the particles is transformed to generate the isothermal Bonnor-Ebert sphere of $T = 200 \text{ K}$ at $n_{\text{H}} = 10^4 \text{ cm}^{-3}$. To boost the collapse, we enhance the mass by 40% when the simulation is started. The resultant total mass of the system is $1.88 \times 10^3 M_{\odot}$. As a result, the initial central density of the cloud is $1.4 \times 10^4 \text{ cm}^{-3}$, and the temperature is 196K assuming barotropic relation. We also add a rigid body rotation to the sphere of angular velocity $\Omega_{\text{rot}} = 2 \times 10^{-14} \text{ s}^{-1}$, that corresponds to the ratio of rotational energy to gravitational energy of $T/|W| \simeq 0.05$. As a result, the specific angular momentum at the outer edge of the cloud ($\sim 2 \text{ pc}$) is $1.2 \text{ pc} \cdot \text{km/s}$, which is consistent with a typical case of collapsing primordial gas in minihalos (Yoshida et al. 2006). At this point, the cloud is spherical, thereby we can freely choose the direction of the angular momentum vector. We choose five directions randomly, to represent slightly different realizations due to the particle distribution. These five realizations are labeled as R1~R5. These five almost identical runs with slightly different realizations can provide the knowledge how chaotic nature of the system can affect the final outcome of the numerical calculation.

We also add anisotropy in particle position, that is, we transform the SPH particle position:

$$x \rightarrow x(1 + \delta \cos 2\phi) \quad (1)$$

$$y \rightarrow y(1 + \delta \cos 2\phi), \quad (2)$$

where x and y denote the Cartesian coordinates of SPH particles perpendicular to the rotation axis, ϕ denotes the azimuthal angle in the xy plane, and $\delta = 0.1$. This perturbation introduces a slightly flattened particle distribution in the xy plane of mode $m = 2$. The initial mass of each SPH particle is $1.8 \times 10^{-3} M_{\odot}$, and it is split into 13 particles (Kitsionas & Whitworth 2002)

when the central density exceeds 10^{10} cm^{-3} , in case the particles are within the distance of $5 \times 10^{-2} \text{ pc}$ from the center. Because the number of neighbor particles in the SPH scheme is chosen as 50, the mass resolution at the central part of the cloud after the split is $2N_{\text{neib}}m_{\text{SPH}} = 0.014M_{\odot}$ (Bate & Burkert 1997), where N_{neib} and m_{SPH} denote the number of neighbor particles and the mass of an SPH particle, respectively. Basic parameters are summarized in Table 1.

When the central density reaches n_{th} , we cut out the central spherical region with $r_{\text{cut}} = 0.015 \text{ pc}$ to follow the subsequent evolution. Larger r_{cut} enables us to follow longer time evolution at a cost of longer computational time. We can follow the evolution until $\sim 1600 \text{ yr}$ after the central core forms for $r_{\text{cut}} = 0.015 \text{ pc}$, after which the absence of an outer envelope reduces the mass accretion rate onto the central region.

2.2. Simulations with sinks

We also perform a sink particle simulation for reference. We perform a run corresponding the same initial conditions of R1. The sink prescription is a standard one. First, we pick up SPH particles where the density exceeds n_{th} and the SPH smoothing length is less than the accretion radius r_{acc} . Here, we set $r_{\text{acc}} = 3 \text{ AU}$, which corresponds to the Jeans length at n_{th} , assuming the barotropic relation. Next, we identify the particles that correspond to the potential local minimum, i.e., find the particles that have lowest gravitational potential among the neighboring particles. Finally, we check that the total energy of the particle and its neighbor particles as a clump is negative. The kinetic energy of the motion of the center of mass is not included in the energy budget. SPH particles that pass all these tests are changed into sink particles. After the sink formation, if SPH particles are closer to a sink particle than the accretion radius r_{acc} and if they are gravitationally bound by the sink in a two-body relationship, they fall onto the sink particle to add their mass and linear momentum to the sinks. Sink-sink mergers are also treated in the same manner as the SPH-sink merger procedure.

3. RESULTS

3.1. Run-away phase

Fig. 1 is an image at the end of the runaway phase. The upper panel shows the density distribution of the run R1. The direction of the spin vector does not affect these results in the runaway collapse phase, therefore we do not plot the results of runs R2~R5. We find a typical distribution for a similarity solution with $\gamma_{\text{eff}} \simeq 1.09$, that leads to the envelope density distribution of $\propto r^{-2.2}$ (e.g. Suto & Silk 1988). This is a well-known behavior of collapsing primordial gas clouds in cosmological simulations (e.g., Yoshida et al. 2006). The lower panel shows the specific angular momentum distribution. The plotted specific angular momentum values are averaged within a sphere of a given radius r , and are normalized by the Kepler rotation value, $j_{\text{Kep}} = \sqrt{GM(r)r}$, where $M(r)$ denotes the mass enclosed within the radius r . We find this ratio is roughly constant at ~ 0.3 in the envelope. These are again consistent with similarity solutions (Saigo & Hanawa 1998).

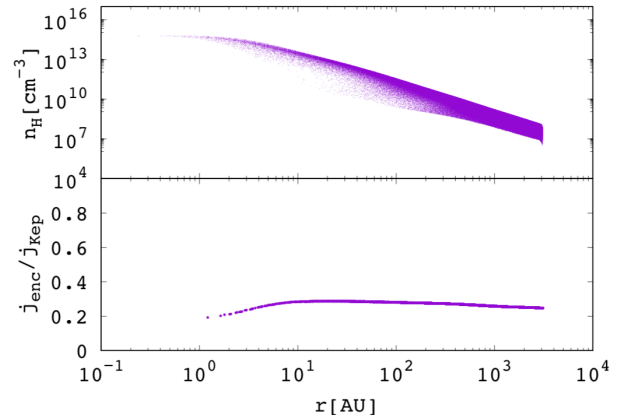


Figure 1. Upper panel: Density distributions for run R1 at the end of the runaway phase. Horizontal axis is the distance from the density peak. Lower panel: Radial distribution of the ratio of the enclosed specific angular momentum and the Kepler value defined as $\sqrt{GM(r)r}$, where $M(r)$ denotes the mass enclosed within the radius r .

3.2. Disk fragmentation in the mass accretion phase

After the central number density reaches $n_{\text{th}} = 10^{15} \text{ cm}^{-3}$, collapse of the central region is stopped by the enhanced pressure owing to the stiff equation of state. Thus, the evolution of the cloud shifts into the mass accretion phase. As an overview of the accretion phase, Fig. 2 shows the time evolution of run R1. The six panels are face-on views of the formed disks, corresponding to times $t = 5, 31, 103, 220, 400, 1100 \text{ yrs}$, respectively. The origin of this time coordinate is the epoch at which the central density exceeds n_{th} for the first time. The purple dots represent the positions of SPH particles, and the green dots denote the positions of identified fragments. The identification procedure is as follows. First, we identify SPH particles of number density higher than $0.9n_{\text{th}}$. Then the SPH particles which are neighbor particles are connected with each other, to create “islands” of dense regions. Finally, if the number of SPH particles in a clump exceeds $6N_{\text{neib}}$, the clump is identified as a fragment, shown by the green dots. This number corresponds to a mass scale slightly higher than three times the Jeans mass at n_{th} . Hence, the identified fragments are not temporarily dense clumps but are gravitationally bound objects.

First, the central dense region reaches the threshold density n_{th} , a dense clump forms (5yr). After a while, the accreted gas forms two spiral arms and the system is still symmetric (31yr). In this phase, the elongated structure is identified as a single clump. This structure arises because of the $m = 2$ mode fluctuation added initially. Then the arms fragment into two fragments so we have three fragments (103 yr). We also see that the symmetry is lost at this stage, and the primary fragment starts departing from the center. This asymmetry is due to the tiny density fluctuation due to the glass-like distribution of the SPH particles. Since the rotation axes of runs R1-R5 are different with each other, so different seed density perturbations are embedded in the runs.

Throughout the evolution of the system, we find vigorous fragmentations of the formed disk as well as the merging of many fragments. We also see that the size of the disks-plus-fragments system is growing with time

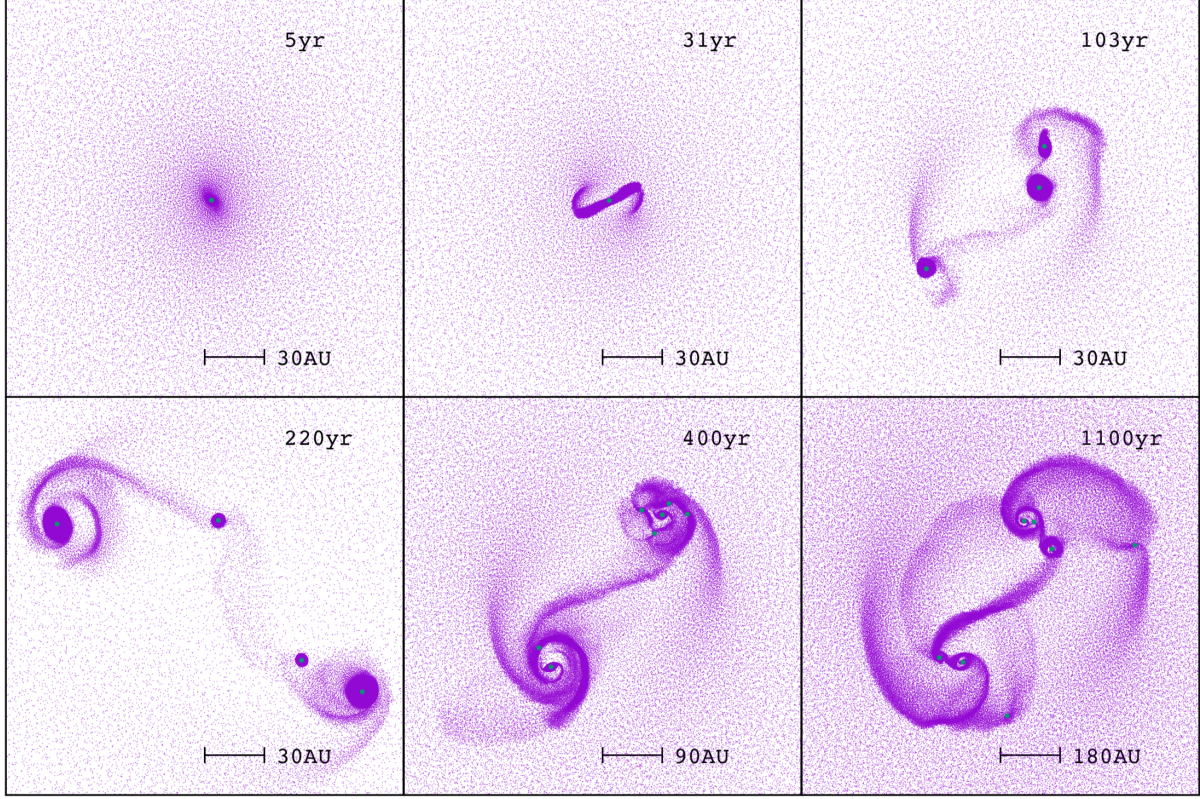


Figure 2. Images of the face-on view of run R1. The corresponding times are (left-to-right, top-to-bottom) $t = 5, 31, 103, 220, 400,$ and 1100 yrs. Green dots denote the position of the identified gas clumps.

(220yr-1100yr). This is because the accreting matter brings in the orbital angular momentum from the envelope. The fragmentation proceeds mainly in the individual accretion disk around each fragment, as discussed in the next subsection. Fig.3 shows the evolution of the cumulative number of fragmentation events (N_+) and mergers (N_-), along with the number of fragments (N_{frag}) for run R1. We find the relation $N_+ \gtrsim N_-$ holds during the evolution, and the slight difference causes a gradual increase of the number of fragments. In Fig.4, the red curve shows the time evolution of the number of formed fragments (ΔN_+) within a short interval of $\Delta t = 30$ yrs. The blue and the green curves show the minimal Toomre Q parameters Q_1 and Q_2 in the disks around the most massive two fragments in run R1. The Q -values are also smoothed over $\Delta t = 30$ yrs. The fragmentation process is episodic, and the fragmentation is active when $Q \lesssim 0.6$. In the superimposed panel, ΔN_+ at every snapshot is plotted against the minimal of Q_1 and Q_2 . We find that in case the fragmentation is active ($\Delta N_+ \gtrsim 1$), the Q value is tend to be less than ~ 0.6 . This condition, $Q < 0.6$, which is derived by Takahashi et al. (2016), corresponds to the condition of gravitational instability of the spiral arms in the disk, while $Q \lesssim 1$ denotes the condition of spiral arm formation. Hence, the present fragmentation process is due to the gravitational instability of the accretion disks.

Fig.5 shows the time of fragmentation vs. the time of merger for all fragments in the runs R1-R5. Because the fragments merge after their birth, all points are located in the upper left region. It is evident that most

of the fragments are just above the diagonal line, where the time of merger almost equals the time of fragmentation. This means the survival times of most fragments are very short compared to the time for the fragmentation. The typical short survival time is roughly $\lesssim 100$ yrs, which is comparable to the typical orbital period of each accretion disk, and is consistent with previous results (e.g. Greif et al. 2012; Hosokawa et al. 2016; Hirano & Bromm 2017). Such a short survival time and the episodic nature of disk fragmentation by gravitational instability leads to the picture discussed by Vorobyov et al. (2013), in which the fragmentation occurs when the disk mass is sufficiently loaded, followed by the rapid migration process. However, we also find 4-6 fragments in each run that survive until the end of the simulations (~ 1600 yrs), shown by the filled marks. Hence, most of the fragments merge at a very short time scale, but some fraction survives. The survived fragments are rare among all of the fragmentation events but exist in all the runs (R1~R5).

3.3. Position of fragmentation

To have a better understanding of the fragmentation process, we assess the two-body specific binding energy e_{pair} for each fragment at its birth with the pre-existing fragments.

The specific two-body binding energy e is described as:

$$e = \frac{1}{2} (\mathbf{v}_{\text{frag}} - \mathbf{v}_{\text{pre}})^2 - \frac{G(m_{\text{frag}} + m_{\text{pre}})}{|\mathbf{r}_{\text{frag}} - \mathbf{r}_{\text{pre}}|} \quad (3)$$

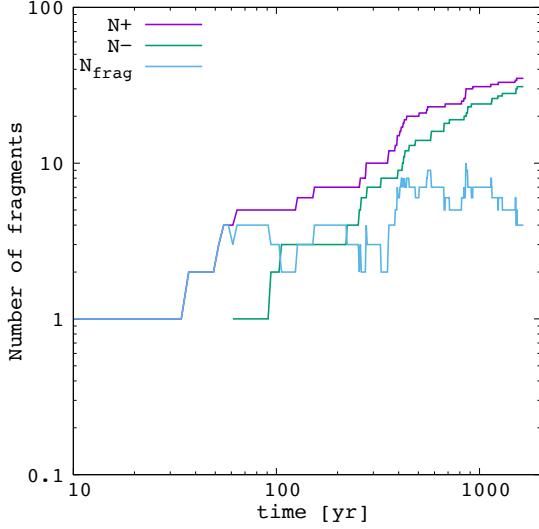


Figure 3. Number of fragments (N_{frag}), cumulative number of formed fragments (N_+) and cumulative number of merger events (N_-) as functions of time in run R1.

where \mathbf{v} , \mathbf{r} , and m denote velocity, position and mass, respectively, whereas the subscripts “frag” and “pre” denote the newly formed fragment and the pre-existing one. We identify all the pre-existing fragments those who have negative e with a newly formed fragment. We define e_{pair} of a newly formed fragment as the two-body binding energy with the nearest pre-existing fragment among the fragments with negative e . In case we find no pre-existing fragment that has negative e with the newly formed fragment, we just use e with the nearest pre-existing fragment. Fig.6 shows e_{pair} for all the newly formed fragments in all runs R1~R5. The horizontal axis shows the time of fragmentation. It is quite clear most of the fragments are bound at their birth by one of the fragments that formed earlier. In fact, 96% of the fragments have negative e_{pair} at their birth. In other words, most of the fragments are born as a companion of another fragment.

To examine the environment of the fragments at their birth more closely, we check whether the pre-existing companions have another companion prior to the newly formed fragment under consideration. In fact, they do have previous companions in 81% of all the fragmenta-

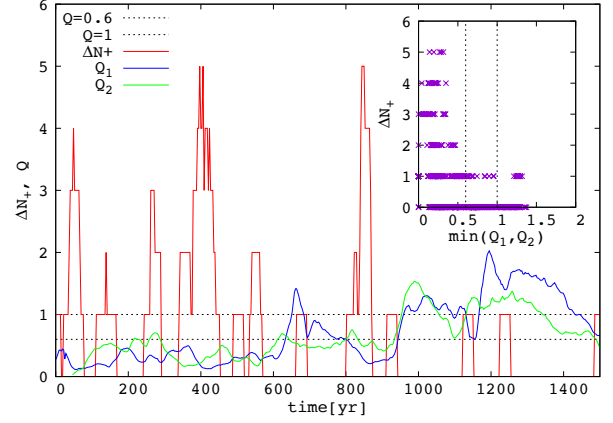


Figure 4. Time evolution of the minimal Toomre Q parameters in the disks around the most massive two fragments (blue and green curves) in run R1. Red curve shows the number of formed fragments within a short interval of $\Delta t = 30$ yrs.

tion events, while 15% of the fragmentation events occur around a single pre-existing fragment. For the 81% events, we plot the distance from the newly born fragments to their companion (we call this a “primary” star), normalized by the distance between the primary star and its pre-existing companion star (hereafter we call this a “secondary”). Note that the terminologies of primary and secondary here are different from the usual definition). In Fig.7, the horizontal axis denotes the mass ratio of the primary and secondary. Note that this ratio can be larger than unity by its definition. For small mass ratio, i.e., in the left side of the figure, the pre-existing secondary is far less massive than the primary. Hence, it does not affect the motion of the newly formed fragment around the primary. This means that the newly formed fragment behaves like a “planet,” as does the secondary. In contrast, in the right side of the figure, the mass of the primary is comparable to or less than that of the secondary. In this case, most of the fragments are born in the neighborhood of the primary. The solid curve denotes the distance from the primary to their shared Lagrangian L1 point defined for the primary and the secondary. The majority of the fragments are located within the L1 radius, that is, they are within the gravisphere of their primaries. Hence, they are born in the accretion disk of the primary. In other words, most of the fragmentation events occur in the accretion disk associated with each fragment, but not in the circumbinary disk nor “circum-multiple” disk.

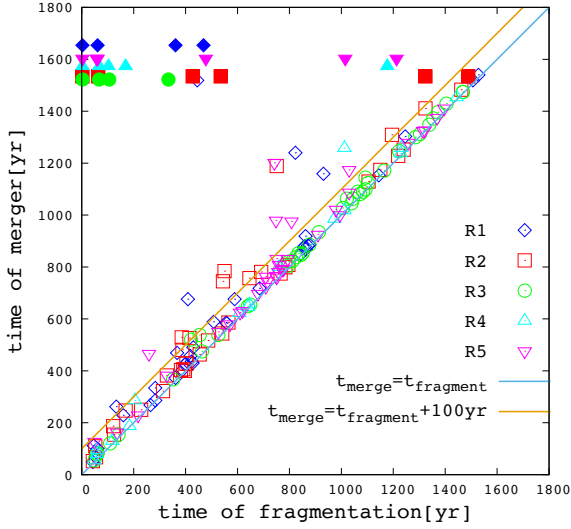


Figure 5. Time of fragmentation vs. time of merger for all fragments in runs R1-R5. Filled symbols show the survived cases, while the open symbols show the merged ones. For the survived cases, the final time of simulation is used instead of the time of merger.

3.4. Number of fragments

In this section, we attempt to model the evolution of N_{frag} by a simple equation and compare it with numerical results. As we discussed in section 3.2, fragmentation occurs when the Q -value of each accretion disk becomes low enough, which implies the fragmentation proceeds in a mass-loading time scale of the disks (Vorobyov et al. 2013). The mass-accretion time scale of the whole system from the envelope is $M(r)/\dot{M}$, where $M(r)$ denotes the enclosed mass within a radius r , and \dot{M} is the total mass accretion rate of the system. This time scale is nearly proportional to t , which is the elapsed time since the first protostar formation. Therefore, we simply assume the fragmentation time scale is proportional to t . Because most of the fragmentation occurs in the accretion disk around each protostar, the formation rate of the fragments is proportional to the number of fragments, N_{frag} , and as a result, we assume the formation

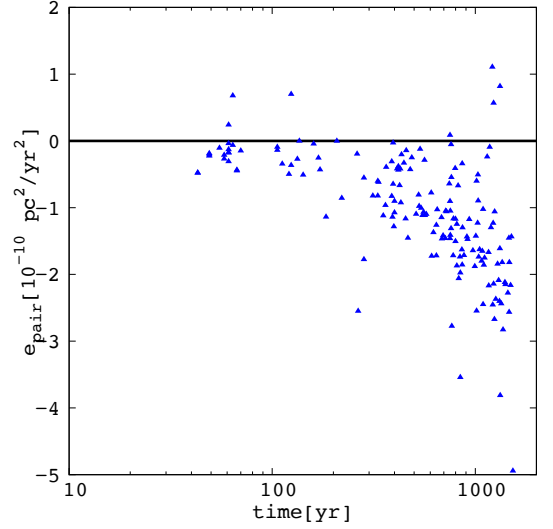


Figure 6. Time vs. e_{pair} for all fragments in the runs R1~R5.

rate of the fragments is

$$\left(\frac{dN_{\text{frag}}}{dt}\right)^+ \propto \frac{N_{\text{frag}}}{t}. \quad (4)$$

It is clear that the merger process proceeds very rapidly (Fig.5), and the merger events quickly follow the fragmentation. Here, we simply assume that the “survival fraction”, which is the fraction of the newly formed fragments to survive the merger processes, is constant. Consequently, the time evolution of N_{frag} is described as

$$\frac{dN_{\text{frag}}}{dt} = p \frac{N_{\text{frag}}}{t}, \quad (5)$$

where p is a non-dimensional constant. This equation can be integrated easily, yielding

$$N_{\text{frag}} \propto t^p. \quad (6)$$

Thus, if we accept this simple equation (5), the number of fragments evolves in a power law solution as a function of time after the formation of the first protostar. In Fig.8, the number of fragments N_{frag} for all non-sink runs (R1~R5) are shown, as well as the results from the run with sinks. For the sink particle simulation the

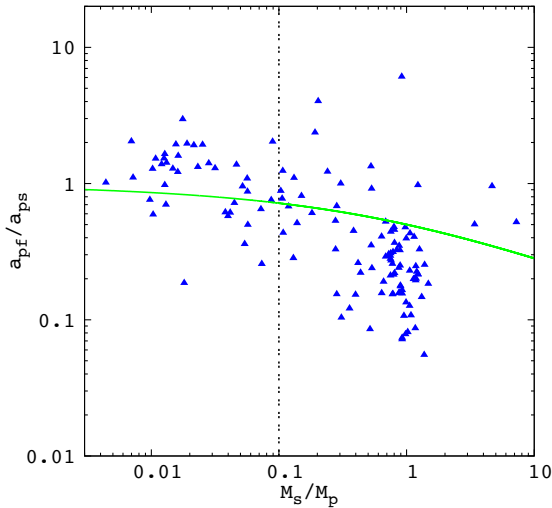


Figure 7. Fragments born in binary systems are plotted on a_{pf}/a_{ps} vs. M_s/M_p plane. Green curve shows the distance from the primary star and the L1 point in the binary system. Vertical dashed line $M_s/M_p = 0.1$ roughly indicates the “planet like” cases. number of sink particles is regarded as N_{frag} . Here, the number is averaged over time intervals for every 50 yrs. In all cases, N_{frag} grows slowly as a function of time, with a scatter due to the continual fragmentation and merger processes. It also should be noted that the differences due to the slightly different realizations (R1-R5) cause some scattering in the results, but it is not large. If we fit the results with a simple power of t , we have $N_{frag} \propto t^{0.3}$, which is consistent with the analytical model.

3.5. Comparison of runs with stiff-EOS and that with sinks

As mentioned in the previous subsection, the results of the sink simulation is also plotted in Fig.8. The time evolution of the number of sinks/fragments are similar with each other, except in the initial phase of $t \lesssim 100$ yrs. In the sink simulation, we find a ring just outside the accretion radius, that becomes gravitationally unstable to form several sinks eventually. This would be an artifact of the present sink procedure. This could be avoided by suppressing the sink formation within two times the sink radius (e.g. Clark et al. 2011). However, these sinks

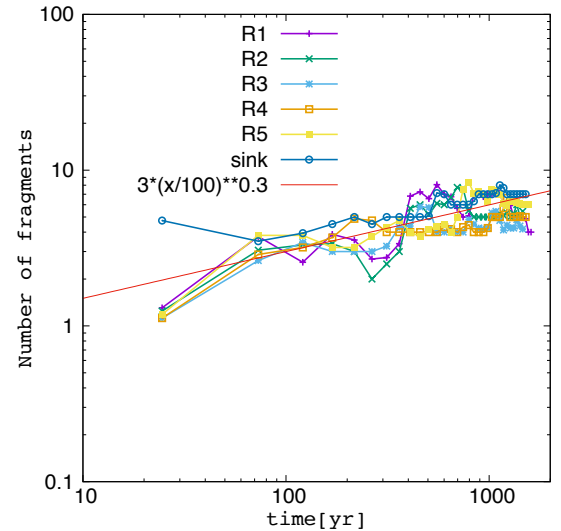


Figure 8. Number of fragments in the non-sink runs (R1~R5) and a sink run (R1)

merge quickly with each other to settle down to the track in Fig.8 consistent with the results from stiff-EOS runs. In addition, we do not observe this kind of artifact in the later phase of the evolution.

Fig.9 shows the time evolution of the total mass accreted onto sink particles or fragments identified in the non-sink simulation R1 (thick curves). The results from two runs are fundamentally same, although there are some deviations with each other. The total mass increase as a power of the elapsed time. The mass of the central singularity in the spherical similarity solution of γ_{eff} is proportional to $t^{4-3\gamma_{eff}}$, which is also shown in the figure as a guide for the eye assuming $\gamma_{eff} = 1.09$.

Fig.9 also shows the mass of all fragments/sinks in each simulation. The basic behaviour of the two runs are same, although the individual evolution is very different. The difference comes from the initial ring fragmentation in the sink simulation that is not found in the stiff-EOS runs and also is due to the chaotic nature of the system. In fact, the number evolution is not identical to each other even in stiff-EOS runs R1-R5(Fig.8).

The final number of this particular two runs are 4 (stiff-EOS) and 7 (sink). On the other hand, the final number

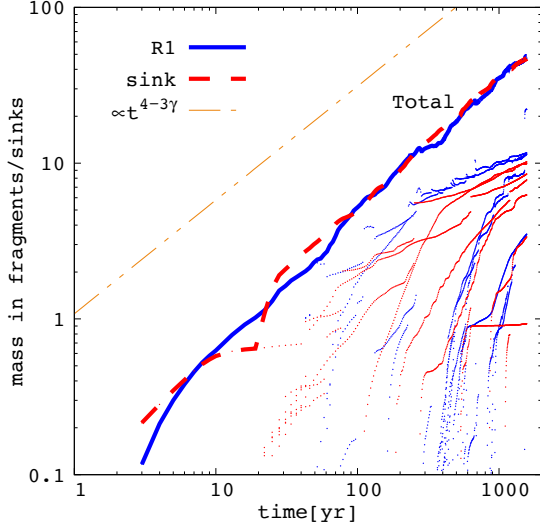


Figure 9. Total mass accreted onto the identified fragments and sink particles as functions of time are shown by thick curves. Mass of the all fragments/sinks are also shown by dots.

of fragments in the stiff-EOS runs (R1-R5) spread over 4 to 6. Hence 7 sink particles seems to be upward, but not so significant.

Overall, the present prescription of the sink simulation do not reproduce the evolution of the individual fragment of the stiff-EOS run, but a rough agreement in the evolution of the total mass/number of the fragments is found.

4. COMPARISON WITH PREVIOUS SIMULATIONS IN THE LITERATURE

We find a simple power-law growth of the number of fragments from our limited sample of simulations. In addition, there are a number of calculations by various authors, although the assumptions of the simulations are different from each other. At first glance, it seems to be difficult to compare these calculations with each other, but according to the scale-free nature of the system, we can compare the results by scaling the time after the formation of the first protostar. The basic equations we solve are

$$\frac{\partial \rho}{\partial t} + \nabla \cdot (\rho \mathbf{v}) = 0,$$

$$\begin{aligned} \frac{\partial \mathbf{v}}{\partial t} + (\mathbf{v} \cdot \nabla) \mathbf{v} &= -\frac{1}{\rho} \nabla P - \nabla \Phi, \\ P &= \kappa \rho^{\gamma_{\text{eff}}}, \quad \nabla^2 \Phi = 4\pi G \rho, \end{aligned}$$

where the variables and constants have ordinary meanings. There are many scales related to the radiative cooling processes as well as to the chemical reactions. In fact, most of the previous works solve the energy equation with gas cooling and heating functions instead of using the barotropic relation. However, it is known that the effective polytropic index is $\gamma_{\text{eff}} \simeq 1.09$ for primordial gas clouds (Omukai & Nishi 1998).

These equations have six variables: $t, \mathbf{r}, \rho, \mathbf{v}, P$, and Φ . These quantities can be replaced by the normalization constant and the non-dimensional variables, as:

$$\begin{aligned} t &= t_0 \tau, \quad \mathbf{r} = r_0 \boldsymbol{\xi}, \quad \rho = \rho_0 \eta, \\ \mathbf{v} &= v_0 \boldsymbol{\zeta}, \quad P = P_0 \sigma, \quad \Phi = \Phi_0 \phi. \end{aligned}$$

Then, the basic equations are rewritten only with the non-dimensional variables, as:

$$\begin{aligned} \frac{\partial \eta}{\partial \tau} + \nabla_{\boldsymbol{\xi}} \cdot (\eta \boldsymbol{\zeta}) &= 0, \\ \frac{\partial \boldsymbol{\zeta}}{\partial \tau} + (\boldsymbol{\zeta} \cdot \nabla_{\boldsymbol{\xi}}) \boldsymbol{\zeta} &= -\frac{1}{\eta} \nabla_{\boldsymbol{\xi}} \sigma - \nabla_{\boldsymbol{\xi}} \phi, \\ \sigma &= \eta^{\gamma_{\text{eff}}}, \quad \nabla_{\boldsymbol{\xi}}^2 \phi = \eta, \end{aligned}$$

if the normalization constants satisfy the following five set of equations:

$$\begin{aligned} t_0 &= \frac{1}{\sqrt{4\pi G \rho_0}}, \quad v_0 = \sqrt{\kappa \rho_0^{\gamma_{\text{eff}} - 1}}, \\ r_0 &= v_0 t_0, \quad \Phi_0 = v_0^2, \quad P_0 = \kappa \rho_0^{\gamma_{\text{eff}}}. \end{aligned} \quad (7)$$

Thus, we have six constants for normalization and five equations. As a result, one constant remains free. Suppose that we have two simulations with different threshold densities $\rho_{\text{th}} (= \mu m_{\text{H}} n_{\text{th}})$ that characterize the sink formation density or the stiffening of the equation of state. We can choose this threshold density as the one free normalization constant in place of ρ_0 . In that case, if the initial condition for the non-dimensional equation is same, the numerical results should be equivalent regarding the scaled variables. In fact, at the onset of the mass accretion phase, the system has converged to the similarity solution, which is almost the same in both of the calculations in terms of the non-dimensional quantities, although some differences could arise from the difference of the numerical methods/implementations or initial conditions. Hence, two distinct calculations with different ρ_{th} should be similar to each other if physical variables are scaled according to the equations (7) with ρ_0 replaced by ρ_{th} . One concern is that sink particle simulations normally introduce not only the threshold density but also the accretion radius. However, the accretion radii r_{acc} are chosen so that they are comparable to, or slightly larger than, the Jeans length estimated at the threshold density ρ_{th} . Considering that the length is scaled by the Jeans length, as in equations (7), the effect due to the choice of r_{acc} seems limited.

Table 4 is the list of numerical simulations in this context so far. In the table, numerical method, threshold density and other specific information are shown.

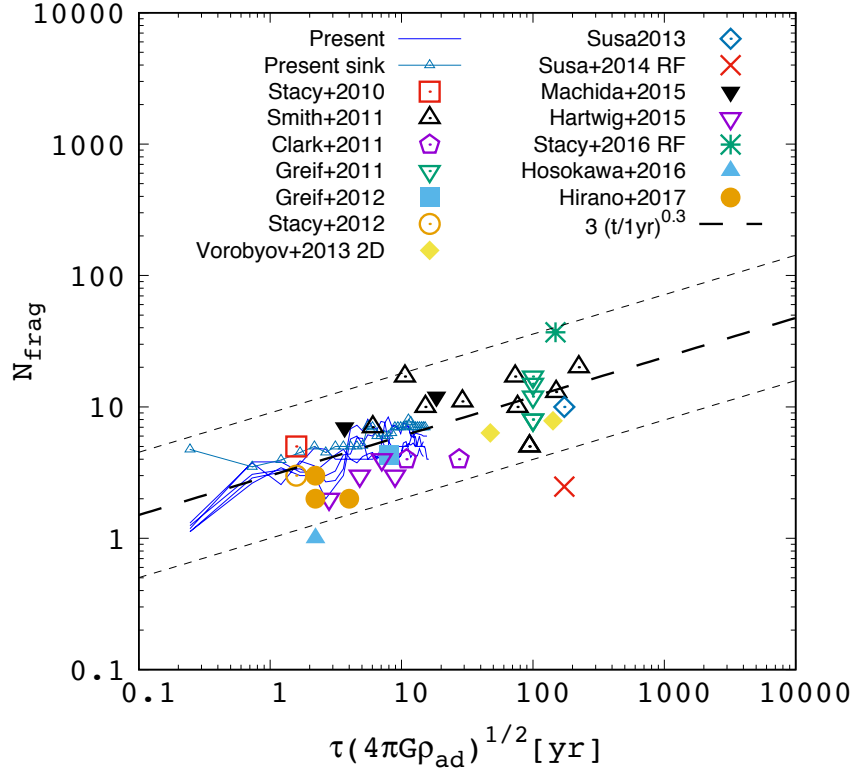


Figure 10. Number of fragments/sinks vs. scaled time. The scaled time is defined as $\tau\sqrt{4\pi G\rho_{\text{ad}}}$. The thick dashed line shows the fit $\propto t^{0.3}$, and the thin dashed lines are guides for the eyes that denote $\times 3$ and $\times 1/3$ of the thick dashed line. Thin blue lines denote the present results smoothed over 50 yrs as in Fig.8, and small triangles with a thin line denote the results of the sink simulation in this work. Open symbols denote the sink simulations (Stacy et al. 2010; Clark et al. 2011; Smith et al. 2011; Greif et al. 2011; Susa 2013; Hartwig et al. 2015b) while the filled marks are for non-sink simulations (Greif et al. 2012; Vorobyov et al. 2013; Hosokawa et al. 2016; Hirano & Bromm 2017). For the case of Vorobyov et al. (2013) we assume $n_{\text{th}} = 10^{14} \text{ cm}^{-3}$, which corresponds to the Jeans length = 6 AU, and the data points are averaged over the first and second 30 kyrs. For Hosokawa et al. (2016), $n_{\text{th}} = 10^{10} \text{ cm}^{-3}$ is assumed. The others show results with radiative feedback (Stacy et al. 2012, 2016; Susa et al. 2014). For Susa et al. (2014), the number is taken from the final time, and the number of fragments are averaged over all the runs. For the studies that include both of the case with/without radiative feedback, the results from the calculations without radiative feedback are chosen. We also tried to plot the results from Riaz et al. (2018), but the elapsed time since the first sink formation is unclear, thereby it is omitted.

Table 2
Previous simulations

Reference	Method	n_{th}	Remark
Stacy et al. (2010)	sink	10^{12}cm^{-3}	Cosmological, 1 halo
Clark et al. (2011)	sink	10^{17}cm^{-3}	Cosmological, 1 halo, 2 snapshots
Greif et al. (2011)	sink	10^{17}cm^{-3}	Cosmological, 5 halos
Smith et al. (2011)	sink	10^{15}cm^{-3}	Cosmological, 5 halos, two snapshots
Greif et al. (2012)	no approx.	10^{19}cm^{-3}	Cosmological, 4 halos, averaged
Stacy et al. (2012)	sink	10^{12}cm^{-3}	Cosmological, 1 halo, RF/NF
Susa (2013)	sink	$3 \times 10^{13}\text{cm}^{-3}$	BE-sphere, 1 cloud, RF/NF
Vorobyov et al. (2013)	1 sink + stiff EOS	10^{14}cm^{-3}	Cosmological, 1 halo, 2D, time averaged
Susa et al. (2014)	sink	$3 \times 10^{13}\text{cm}^{-3}$	Cosmological, 59 halos, RF, averaged
Machida & Nakamura (2015)	stiff EOS	10^{19}cm^{-3}	BE-sphere, 1 cloud, time averaged
Hartwig et al. (2015b)	sink	10^{17}cm^{-3}	Cosmological, 4 halos
Hosokawa et al. (2016)	cut cooling	$10^{10} - 10^{12}\text{cm}^{-3}$	Cosmological, 5 halos, RF/NF, polar coord.
Stacy et al. (2016)	sink	10^{15}cm^{-3}	Cosmological, 1 halo, RF
Hirano & Bromm (2017)	cut cooling	$10^{10}, 10^{13}, 10^{15}\text{cm}^{-3}$	Cosmological, 1 halo

Note. — "RF" and "NF" means the simulations with/without UV radiative feedback. "averaged" denotes that the number in Fig.10 is the averaged number over halos. "time averaged" means the provided time evolution in the reference is time averaged to put on the figure.

Fig.10 shows the number of fragments as a function of time scaled by the free-fall time of the threshold density. Simulations in the literature (4) are shown on the plot with different symbols. We choose the threshold number density $n_{\text{ad}} = 10^{19} \text{ cm}^{-3}$ as the standard, which is the critical density above which the dense core becomes physically adiabatic in the highest resolution simulation (Greif et al. 2012). Hence, we define the scaled time as $\tau\sqrt{4\pi G\rho_{\text{ad}}}$, where $\rho_{\text{ad}} = \mu m_{\text{H}} n_{\text{ad}}$. Thus, the scaled time of the data point from Fig. 10 in Greif et al. (2012) is their physical time (8 yrs). In other words, the scale time can be regarded as the "real" physical time.

We find that the results from a number of simulations are fundamentally consistent with each other, although they use different numerical methods, initial conditions, cooling functions, and equations of state. In fact, the data points from the cosmological simulation by Smith et al. (2011) imply that the dependence on the initial conditions already produces the diversity of a factor of ~ 4 . Thus, this remarkable agreement in this plot tells that the differences caused by the variety of the schemes are at least comparable to the scatter of the results due to the different initial conditions.

We note that the data from Susa et al. (2014) should be regarded as a lower limit because they took into account the radiative feedback by the protostars, which shut off the fragmentation process in the disk. Stacy et al. (2012, 2016) also took into account the radiative feedback, but their integrated time is 5000 yrs, which corresponds to the onset of the feedback. Hence, the effect of suppressing the fragmentation is limited. Considering the diversity due to the initial conditions, the results could be compared with the other calculations without radiative feedback. The data from Hosokawa et al. (2016) also should be considered as a lower limit, because it used polar coordinates, which tend to have less resolution at the outer part of the disk. The lower resolution results in a smaller fragmentation process in the disk.

5. DISCUSSION

We can extrapolate the relation $N_{\text{frag}} \propto t^{0.3}$ to several thousand years, the beginning of the radiative feedback from massive protostars. We find the number of fragments is 10 \sim 100 at that epoch. This number is somewhat larger than expected, especially from non-sink simulations. One possible reason for this is that non-sink simulations normally follow the evolution of the system for a shorter time than the sink simulations, so they predict fewer fragments. If we regard the feedback as strong enough to shut off the disk fragmentation/merger, we arrive at the final number of the protostars at that epoch i.e. 10-100.

However, the previous studies (Hosokawa et al. 2011, 2016; Susa 2013; Stacy et al. 2016) predict that the effects of radiative feedback becomes prominent $10^3 - 10^4$ yrs after the formation of the first protostar, not in good agreement. If the photoevaporation of the disk proceeds slowly and the fragmentation/merger processes continue to much later time, the expected number of fragments could be different. It is a disk fragmentation problem under UV radiation field, in which the outcome do not scales by the relation discussed in the previous section. Thus, it has to be investigated in the future studies.

In any case, we have to extend our non-sink/sink simulations *without* UV feedback to several thousand years in scaled time to confirm the $N_{\text{frag}} \propto t^{0.3}$ trend all the way to the onset of the radiative feedback. Then, the simulations should be followed by calculations with UV feedback to obtain the final mass distributions, binary frequencies, and so forth.

Another complexity is coming from the magnetic field associated with the turbulence. Very high resolution simulations (Sur et al. 2012; Federrath et al. 2011; Turk et al. 2012) as well as the analytic calculations using Kazantsev equation (Schleicher et al. 2010; Schober et al. 2012) show that the minihalo is turbulent and the initial seed magnetic field is easily amplified to the equipartition level. Because of the strong coupling between the magnetic field and the gas in primordial gas (Maki & Susa 2004, 2007; Susa et al. 2015; Higuchi et al. 2018), B-field is not dissipated at the Jeans scale, to be amplified efficiently. The effects of magnetic field on the PopIII star formation has been investigated by Machida & Doi (2013), where they find that the circumstellar disk formation is suppressed in the presence of equipartition level B-field, because of the efficient angular momentum transportation by the magnetic breaking. As a result, no fragments are found. However they assume a coherent field parallel to the rotation axis, which is quite different from the turbulent magnetic field expected in the minihalos². On the other hand Seifried et al. (2012) reported that turbulence can circumvent the magnetic breaking catastrophe in the context of the present-day star formation. Thus, the effects of turbulent magnetic field on the PopIII disk fragmentation is still an open question, which should be addressed in the future.

6. SUMMARY

We perform cloud collapse simulations with a barotropic equation of state derived from the one-zone model of the gravitationally contracting primordial gas cloud, to mimic the formation of PopIII stars. We find growing disk-like structures after the formation of the first fragment, followed by the rapid fragmentation of the disk and the merger of the fragments when the disk becomes massive enough to be gravitationally unstable. We find that most of the fragmentation events occur in the accretion disk around individual fragments. These results suggest a simple analytical model of the evolution of the number of fragments that predicts a power-law growth of them. In fact, we find that the number of fragments slowly increases with time, following the relation $N_{\text{frag}} \propto t^{0.3}$. We also perform a simulation with standard sink particles, where the number and total mass of sink particles are in rough agreement with those of the stiff equation of state runs. Finally, we compare the number of fragments with other published results, by scaling the simulated time according to the notion of the scale-free nature of the system. Consequently, we find a good agreement among most of the calculations so far. The present results combined with the studies in the literature imply that the population III stars are not born as single stars, but in a multiple system.

² Latif & Schleicher (2016) discussed the $\alpha\Omega$ dynamo process in the accretion disk, where they find the coherent field could be generated from the turbulent field.

HS thanks the anonymous referee for careful reading and constructive comments., T. Hosokawa, M. Machida, G. Chiaki, S. Hirano and T. Hartwig for fruitful discussions. We thank the support by Ministry of Education, Science, Sports and Culture, Grant-in-Aid for Scientific Research Nos. 17H02869, 17H01101, and 17H06360.

REFERENCES

- Abel, T., Bryan, G. L., & Norman, M. L. 2002, *Science*, 295, 93
- Bate, M. R., & Burkert, A. 1997, *MNRAS*, 288, 1060
- Bromm, V., Coppi, P. S., & Larson, R. B. 2002, *ApJ*, 564, 23
- Chiaki, G., Susa, H., & Hirano, S. 2018, *MNRAS*, 475, 4378
- Clark, P. C., Glover, S. C. O., Smith, R. J., et al. 2011, *Science*, 331, 1040
- Chen, K.-J., Whalen, D. J., Wollenberg, K. M. J., Glover, S. C. O., & Klessen, R. S. 2017, *ApJ*, 844, 111
- Federrath, C., Sur, S., Schleicher, D. R. G., Banerjee, R., & Klessen, R. S. 2011, *ApJ*, 731, 62
- Fuller, T. M., & Couchman, H. M. P. 2000, *ApJ*, 544, 6
- Greif, T. H., Bromm, V., Clark, P. C., et al. 2012, *MNRAS*, 424, 399
- Greif, T. H., Springel, V., White, S. D. M., et al. 2011, *ApJ*, 737, 75
- Griffen, B. F., Dooley, G. A., Ji, A. P., et al. 2018, *MNRAS*, 474, 443
- Haiman, Z., Thoul, A. A., & Loeb, A. 1996, *ApJ*, 464, 523
- Hartwig, T., Bromm, V., Klessen, R. S., & Glover, S. C. O. 2015, *MNRAS*, 447, 3892
- Hartwig, T., Glover, S. C. O., Klessen, R. S., Latif, M. A., & Volonteri, M. 2015, *MNRAS*, 452, 1233
- Higuchi, K., Machida, M. N., & Susa, H. 2018, *MNRAS*, 475, 3331
- Hirano, S., Hosokawa, T., Yoshida, N., et al. 2014, *ApJ*, 781, 60
- Hirano, S., Hosokawa, T., Yoshida, N., Omukai, K., & Yorke, H. W. 2015, *MNRAS*, 448, 568
- Hirano, S., & Bromm, V. 2017, *MNRAS*, 470, 898
- Hosokawa, T., Omukai, K., Yoshida, N., & Yorke, H. W. 2011, *Science*, 334, 1250
- Hosokawa, T., Hirano, S., Kuiper, R., et al. 2016, *ApJ*, 824, 119
- Ishigaki, M. N., Tominaga, N., Kobayashi, C., & Nomoto, K. 2018, *ApJ*, 857, 46
- Ishiyama, T., Sudo, K., Yokoi, S., et al. 2016, *ApJ*, 826, 9
- Jarvis, B. C. L. et al. 2011, *ApJS*, 192, 14
- Kitsionas, S., & Whitworth, A. P. 2002, *MNRAS*, 330, 129
- Latif, M. A., & Schleicher, D. R. G. 2016, *A&A*, 585, A151
- Machida, M. N., & Doi, K. 2013, *MNRAS*, 435, 3283
- Machida, M. N., & Nakamura, T. 2015, *MNRAS*, 448, 1405
- Magg, M., Hartwig, T., Agarwal, B., et al. 2018, *MNRAS*, 473, 5308
- Magg, M., Klessen, R. S., Glover, S. C. O., & Li, H. 2019, *arXiv:1903.08661*
- Maki, H., Susa, H. 2004, *ApJ*, 609, 467
- Maki, H., Susa, H. 2007, *PASJ*, 59, 787
- Nishi, R., & Susa, H. 1999, *ApJL*, 523, L103
- Omukai, K., & Nishi, R. 1998, *ApJ*, 508, 141
- Riaz, R., Bovino, S., Vanaverbeke, S., & Schleicher, D. R. G. 2018, *MNRAS*, 479, 667
- Saigo, K., & Hanawa, T. 1998, *ApJ*, 493, 342
- Schleicher, D. R. G., Banerjee, R., Sur, S., Arshakian, T. G., Klessen, R. S., Beck, R., & Spaans, M. 2010, *arXiv:1003.1135*
- Schober, J., Schleicher, D., Federrath, C., et al. 2012, *ApJ*, 754, 99
- Seifried, D., Banerjee, R., Pudritz, R. E., & Klessen, R. S. 2012, *MNRAS*, 423, L40
- Smith, R. J., Glover, S. C. O., Clark, P. C., Greif, T., & Klessen, R. S. 2011, *MNRAS*, 414, 3633
- Smith, B. D., Wise, J. H., O’Shea, B. W., Norman, M. L., & Khochfar, S. 2015, *MNRAS*, 452, 2822
- Stacy, A., Greif, T. H., & Bromm, V. 2010, *MNRAS*, 403, 45
- Stacy, A., Greif, T. H., & Bromm, V. 2012, *MNRAS*, 422, 290
- Stacy, A., Bromm, V., & Lee, A. T. 2016, *MNRAS*, 462, 1307
- Sur, S., Federrath, C., Schleicher, D. R. G., Banerjee, R., & Klessen, R. S. 2012, *MNRAS*, 423, 3148
- Susa, H. 2006, *PASJ*, 58, 445
- Susa, H., & Umemura, M. 2004, *ApJ*, 600, 1
- Susa, H. 2013, *ApJ*, 773, 185
- Susa, H., Hasegawa, K., & Tominaga, N. 2014, *ApJ*, 792, 32
- Susa, H., Doi, K., & Omukai, K. 2015, *ApJ*, 801, 13
- Suto, Y., & Silk, J. 1988, *ApJ*, 326, 527
- Takahashi, S. Z., Tsukamoto, Y., & Inutsuka, S. 2016, *MNRAS*, 458, 3597
- Tanaka, S. J., Chiaki, G., Tominaga, N., & Susa, H. 2017, *ApJ*, 844, 137
- Turk, M. J., Oishi, J. S., Abel, T., & Bryan, G. L. 2012, *ApJ*, 745, 154
- Vorobyov, E. I., DeSouza, A. L., & Basu, S. 2013, *ApJ*, 768, 131
- Yoshida, N., Abel, T., Hernquist, L., & Sugiyama, N., 2003, *ApJ*, 592, 645
- Yoshida, N., Omukai, K., Hernquist, L., & Abel, T. 2006, *ApJ*, 652, 6